Journal Name

Indentation of graphene nano-bubbles

Fahim Faraji,[a,b,d] Mehdi Neek-Amal,[b,c] Erik C. Neyts,[a,d] and François M. Peeters[b,d]

Molecular dynamics simulations are used to investigate the effect of an AFM tip when indenting graphene nano bubbles filled by a noble gas (i.e. He, Ne and Ar) up to the breaking point. The failure points resemble those of viral shells as described by the Föppl–von Kármán (FvK) dimensionless number defined in the context of elasticity theory of thin shells. At room temperature, He gas inside the bubbles is found to be in the liquid state while Ne and Ar atoms are in the solid state although the pressure inside the nano bubble is below the melting pressure of the bulk. The trapped gases are under higher hydrostatic pressure at low temperatures than at room temperature.

1 Introduction

Van der Waals heterostructures consist of atomically flat thin materials which adhere to each other by van der Waals attraction[1]. The presence of contaminants is inevitable while fabricating these heterostructures. Contaminants may include several materials spanning from e.g. noble gases to water and hydrocarbons. Strong adhesion between the layers may squeeze out the contaminants into nano scale bubbles[2–4]. These bubbles were regarded as a signature of the adhesion between the layers. They were used in the investigation of the elastic properties of two-dimensional materials and to study the properties of highly confined materials[5–10].

AFM nano indentation has been used to study the mechanics of thin materials including nano bubbles, as well as viral shells such as protein aggregates[2,11]. Nano indentation may also be used to determine the hydrostatic pressure of the materials trapped inside the bubbles. An important question is: up to which size the bubble response against indentation can be described by continuum theories?

Here, we use molecular dynamics (MD) simulations to study the nano indentation of graphene nano bubbles. The noble elements He, Ne and Ar were used as trapped materials. We found that the bubbles exhibit structural failure upon high indentation. The failure deformation points and the linear response regime are well described by continuum theories. Furthermore, the bubbles exhibit resilience against periodic deformations prior to their failure points. The hydrostatic pressure of the trapped material was found to be highly sensitive to temperature, which was mostly due to the influence of temperature on the bubbles' geometry. In contrast to He, Ne and Ar elements show crystalline structure below their melting pressure at room temperature which is a distinct signature of the effect of very strong confinement on the properties of the trapped materials.

2 Simulation details

The simulated system consists of a substrate made of Platinum (Pt-111), a graphene sheet above the substrate, and a noble material trapped between the substrate and graphene. The substrate dimensions was taken to be $10 \times 10 \times 1$ nm and the graphene sheet dimensions are 7.5×7.5 nm. At the start of the simulation, the graphene central region was manually lifted to form an artificial bubble which was filled by one of the three noble materials: He, Ne and Ar. A spheroidal surface tip with sphere radius of 2 nm (which corresponds to the smallest commercial AFM tip) made of silicon was placed above the graphene bubble. The tip had a FCC atomic structure with a lattice constant of 5.43 Å. Fig. 1 shows schematically the simulated system.

EAM[12] and AIREBO[13] potentials were used for the substrate and the graphene, respectively. The cut-off radii of the AIREBO potential were set to 0.2 nm, which has been demonstrated to eliminate non-physical strain hardening[14,15] during strong stretching in graphene[16,17]. We examined the potential by stretching a pristine graphene sheet and observed brittle breaking with a fracture stress of ~ 107 GPa that agrees with the experimental results[18]. The trapped materials, as well as the van der Waals interactions among all elements were modelled using the 12/6 Lennard-Jones (LJ) potential. The employed LJ coefficients for different materials are summarised in table 1, while the cross parameters were calculated using the Lorentz-Bertholet mixing rule. The van der Waals interactions were cut off at 9.8 Å.

The graphene and the trapped materials were initially subjected to an energy minimisation using the conjugate-gradient

[a] PLASMANT, Department of Chemistry, University of Antwerp, Universiteitsplein 1, 2610 Antwerp, Belgium

[b] Condensed Matter Theory, Department of Physics, University of Antwerp, Groenenborgerlaan 171, 2020 Antwerp, Belgium

[c] Department of Physics, Shahid Rajaee Teacher Training University, 16875-163 Tehran, Iran

[d] Center of Excellence NANOlab, University of Antwerp, Groenenborgerlaan 171, 2020 Antwerp, Belgium
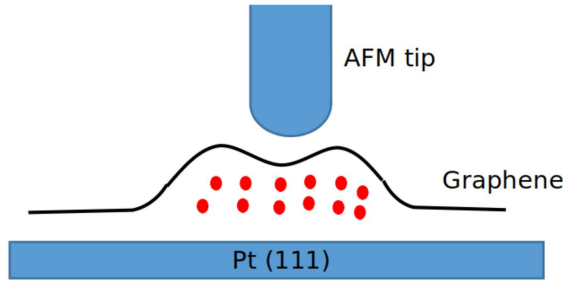
Fig. 1 Schematic of the nano bubble system. Trapped materials are confined between the Pt substrate and the graphene sheet. A spheroidal tip was placed above the bubble which caused deformation of the graphene sheet.

Table 1 Parameters for the interaction potentials

Atom type	σ_i(Å)	$\varepsilon_i/k_B(K)$	Ref.
Pt	2.54	7910	ref. 23
C	3.41	28	ref. 24
He	2.55	10	ref. 25
Ne	2.82	32	ref. 25
Ar	3.47	114	ref. 25
Si	3.33	103	ref. 23

algorithm[19]. Then, their temperature was gradually increased from zero to the desired temperature after which NVT simulation was continued until the bubbles geometry, namely, its radius and maximum height, exhibited a steady configuration. Next, the tip was moved down with a constant velocity of 0.2 Å/ps until the tip touched the graphene and deformed it. We found the tip speed results in a strain rate of $\sim 9 \times 10^{-4}$ ps^{-1} in the graphene bond length (in the area under the indentation), which is typical in MD simulations[20]. During the simulations, we reduced the tip speed until we observed that further reducing the speed had little impact on the results. To explore the effect of temperature, we repeated the simulations at two temperatures including room temperature (T = 300K), and a low temperature (T = 5K). The newtonian equations of motion were integrated using the velocity-verlet algorithm with a time step of 1 fs. All simulations were carried out using the Lammps[21] package. Graphical snapshots and movies in the supplementary information are created using the Ovito software[22].

3 The bubble geometry

Once the bubbles exhibited a steady geometry, we measured the radius and maximum height of the bubbles filled by He, Ne or Ar at two temperatures: 5K and 300K. Moreover, to examine different bubble dimensions for each trapped element, the simulations were performed for two different number of trapped atoms $N_t =$ 800 and $N_t = 1100$. Initially, the tip was placed sufficiently above the bubbles (more than the LJ cut-off radius) so that it did not affect the bubbles prior to the indentation. To measure the bubble radius and height, we plotted the cross section of the graphene sheets and heuristically defined the radius from the points where graphene started to move out of plane and the height was defined

Table 2 The radius and height of the graphene nano bubbles for different trapped elements, temperature and number of trapped atoms N_t

Gas/N_t	T = 300K			T = 5K		
	R(Å)	h(Å)	h/R	R(Å)	h(Å)	h/R
He/800	28.60	6.41	0.22	28.10	6.13	0.22
Ne/800	33.50	7.32	0.22	31.89	7.99	0.25
Ar/800	44.61	9.11	0.20	40.99	9.22	0.22
He/1100	33.48	7.33	0.22	33.33	7.42	0.23
Ne/1100	39.70	7.91	0.20	37.18	8.87	0.24
Ar/1100	48.21	9.92	0.21	46.60	10.92	0.23

as the maximum vertical distance of graphene from the plane it defines away from the bubble.

The results for the bubble radius and maximum height for different trapped materials, as well as for the two temperatures and N_t are summarised in table 2. In general, the bubbles seem to follow the universal scaling in their height to radius aspect ratio[2]. It is worth mentioning that the bubbles' radius are sufficiently larger than 1 nm below which we recently have shown that a breakdown in the universal scaling is envisaged[26]. Notice that the aspect ratio values are in quantitative agreement with experiment (see Table (1) of ref. 26 for the large bubble regime). When comparing the bubbles radius for the same N_t, the Ar bubbles have the largest radius, followed by Ne and then He bubbles. We attribute this to the van der Waals radius of the trapped elements which is the largest for Ar and the smallest for He (see table 1). For the same N_t and trapped material, the bubble acquire a larger radius at room temperature as compared to the low temperature results. This can be related to the higher adhesion energy between graphene and the substrate at low temperatures. Specifically, when temperature is high, the graphene atoms have higher kinetic energy with stronger vibrations, thereby having lower effective adhesion to the substrate. This resembles the effect of temperature in the standard capillary phenomenon. Therefore, at higher temperatures when the adhesion between graphene and the substrate (γ_{SG}) is lower, the trapped materials could detach the graphene sheet from the substrate more easily, thereby creating bubbles with a larger radius.

For the same trapped material and N_t, the low temperature bubbles exhibit higher maximum heights. To understand this, we should note that the bubbles boundaries are not clamped in the simulations, yet it is the interplay between γ_{SG} and the trapped materials hydrostatic pressure which determines the bubbles volume. The pressure is in turn influenced by the adhesion energy[2]. Our calculations show that the hydrostatic pressure of the trapped materials is surprisingly larger at low temperature than at room temperature (see the trapped materials: pressure and aggregation state section). Thus, when the bubbles exert higher pressures on the trapped materials at low temperatures, and concurrently, exhibit lower radius, it will lead to higher maximum heights as can be seen in table 2. This is especially noteworthy as at higher temperature, one would expect a higher maximum height because gas atoms have larger mobility and their structures are more out-of-plane[26]. Nevertheless, pressure induced by enhanced adhesion dominates such that the maximum height is higher at low
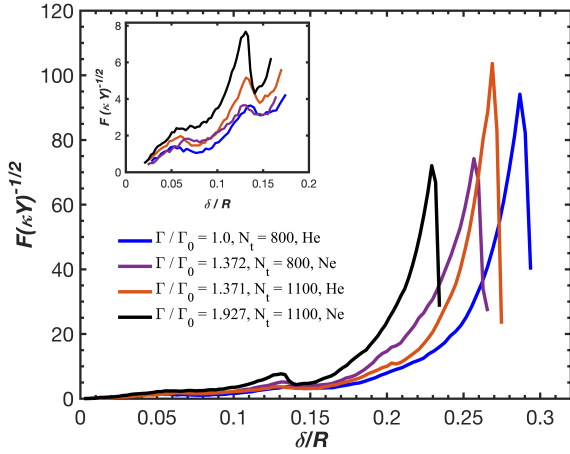
Fig. 2 The force applied on the tip versus the bubbles deformation. The bubbles break at high deformations. The failure points can be described by Föppl–von Kármán (FvK) dimensionless number $\Gamma = \frac{YR^2}{\kappa}$. The inset magnifies the region of the partial drops associated with buckling transitions.

temperature.

Further, if we accept that the trapped materials pressure is given by $P = \frac{4\pi\gamma}{5 c_v h_{max}}$ (see Eq. (23) of ref. 2), where c_v is a constant (≈ 1.7) which depends on the graphene poisson ratio, we find that the adhesion energy γ will be higher at low temperature to the extent that it compensates for both the higher pressure and maximum height. The latter equation was obtained by analytically minimizing the total energy of the nano-bubble system with respect to the bubble radius and maximum height, and empirically correlating the free parameters to the experimental data[2]. The total energy includes the elastic energy of the deformed graphene, the free energy of the trapped materials, and the vdW energy necessary to separate the graphene from the substrate[2].

4 Indentation force-deformation curves

Once the bubbles have reached their steady geometrical shape, we start moving down the tip. After touching graphene, the tip deformed the bubble until the point that the bubble eventually breaks and the graphene sheet ruptures. Snapshots from MD are shown in supplementary Fig. S1-S4, and supplementary movie 1 which demonstrate the deformation and failure of the bubble as a result of the indentation. Fig. 2 illustrates the variation of the vertical force applied on the tip as the tip moves down and deforms the bubble at room temperature. Here, the horizontal axis is the indentation depth (δ) normalised by the corresponding bubble radius (R), and the vertical axis is the vertical component of the total force on the tip normalised by ($\sqrt{\kappa Y}$). Here, κ is the bending stiffness and Y is the two-dimensional Young modulus of the graphene sheet which at room temperature are equal to $\kappa = 0.24$ nN-nm and $Y = 340$ N/m.

As expected, the curves are ascending, that is, the indentation force increases with increased deformation. It can be seen that the curves are initially linear, and gradually become nonlinear for higher deformations. At least two partial drops (at $\delta/R \approx 0.06$

and 0.13) are discernible in the curves after which the curves become highly nonlinear followed by a dramatic drop. The partial drops in the curves are associated with the points where the energy of two different shapes of the graphene nanobubble cross each other which are commonly referred to as buckling transitions in the engineering literature[27] (see the inset of Fig. 2). The dramatic drop of the curves at high deformation are attributed to the failure of the graphene bubble.

Being similar in nature to pressurised vessels, one can ask oneself whether elasticity theory of thin shells[28] (TST) is helpful in interpreting the indentation of our bubbles. One important dimensionless number in TST is the so-called Föppl–von Kármán (FvK) number $\Gamma = \frac{YR^2}{\kappa}$ which for a perfect sphere represents the ratio of the magnitude of the in-plane stretching to the out-of-plane bending forces. In our problem, κ and Y are the same for all bubbles, so the bubble radius solely determines the FvK number (Γ). Using the aforementioned values for κ and Y, the FvK number for our He bubble with $N_t = 800$ at room temperature is calculated as $\Gamma = 11,588$ (which we will refer to Γ_0 hereinafter). The FvK values for the other bubbles normalised to Γ_0 are given as legend in Fig. 2. Interestingly, we see that the failure point of the bubbles can be predicted from their FvK number: the higher the FvK number the lower δ/R for bubble failure. This is valid to the extent that the FvK number of the He bubble with $N_t = 1100$ is quite close and slightly higher than that of the Ne bubble of $N_t = 800$, and the He bubble fails for a slightly lower δ/R. Interestingly, this description is similar to what has been reported in experiments on failure of viral shells[29]. Notice that, the failure force is not affected by the FvK number but it is affected by the trapped material.

Similar curves are found for low temperature (T = 5K) which is illustrated in supplementary Fig. S5. Contrary to room temperature, all the curves fail almost at the same δ/R (≈ 0.27). The Γ values in the legend of Fig. S1 were calculated based on the κ and Y values at room temperature. Basically, these material properties depend on temperature, and specially in the case of the bending stiffness, the issue is still under debate and the literature on it is controversial[30–32]. To further investigate this issue, we examined the local strain rates of Ne bubbles with $N_t = 800$ and $N_t = 1100$ at room temperature and low temperature. Supplementary Figs. S6-S9 illustrate strain rates of the bond length across the graphene sheet for these four bubbles just before the graphene sheet failed. The maximum local strain for $N_t = 800$ bubbles is larger than for $N_t = 1100$ bubbles at both temperatures (see the maximum strain rate in the colour bars next to the contour plots). While the precise quantitative values of the local strain rates highly depend on the failure definition, as well as how often the MD data are extracted, the difference between the maximum local strain rates associated with the two N_t numbers is higher at low temperature than at room temperature. The difference at low temperature is four times larger. Therefore, at room temperature, bubbles rupture at relatively close deformations, so that when the deformation rate is normalised with the bubble radiuses (x-axis of Fig. 2), the difference between bubbles of different diameters (and consequently different FvK numbers) will be readily apparent. On the contrary, the failures at low tempera-

ture occur at different deformations such that after normalisation, the influence of deformation is canceled out by the influence of radius, and the curves drop at the same breaking point.

Additionally, it is evident that the maximum local strain rates are higher at low temperatures than at room temperatures (Figs. S8 and S9 compared to Figs. S6 and S7). It is in accordance with the fact that fracture stress of graphene increases with decreasing temperature[33]. In order to explain why the maximum strain rates at room temperature are close to each other as opposed to the results at low temperatures, we attribute it to graphene's increased flexibility at room temperature. By having ripples with enhanced amplitudes at room temperature, graphene becomes more adaptable, so that the area under stress in both N_t numbers becomes similar. At low temperature, graphene becomes rigid and N_t numbers (and radiuses) begin to show their influence. It is worth noting that at both temperatures, the influence of N_t numbers is more pronounced at the bubble edges rather than the stress area (see supplementary Figs. S10 and S11). A quantitative investigation of how the breaking point is sensitive to the changes of FvK number over a continuous temperature range is beyond the scope of the current work. Nevertheless, we expect that the sensitivity gradually decreases from room temperature to a point of insensitivity at low temperature. It is envisioned that at higher temperatures, the sensitivity will increase until a saturation asymptote.

Lastly, we investigated the reversibility of the deformations, and whether or not our graphene nano bubbles are vulnerable against periodic indentations, similar to the concept of fatigue. For this purpose, we applied a cycling back and forth indentation to the Ne bubble of $N_t = 800$ at room temperature until the deformation $\delta/R = 0.20$ which is before the bubble failure, yet after the two partial buckling transitions. Fig. 3 illustrates the resulted force-deformation curves after 50 cycling indentations. The bubble indeed exhibits resilience against fatigue while clear hysteresis can be observed. The hysteresis starts to develop after the first bucking transition, before which the deformations are reversible for small indentation. We also examined the fatigue and reversibility for the same bubble at low temperature. Its graph is similar to Fig. 3 and is given in supplementary Fig. S12.

5 Elasticity theory of thin shells (TST)

For small indentations when the relation between the indentation force and the deformation is still linear, TST predicts the total free energy H of a pressurised shell of a perfect sphere system as

$$H = \int dS \left\{ \frac{1}{2}\kappa(\Delta\zeta)^2 + \frac{1}{2}\tau(\zeta)^2 + \frac{1}{2}Y\left(\frac{2\zeta}{R}\right)^2 \right\} \quad (1)$$

where $\zeta = \zeta(r)$ is the indentation profile, τ the osmotic pressure, and dS the surface differential. Minimizing the energy with respect to the indentation profile yields $F.R \approx 8\sqrt{\kappa Y}\zeta$ for the case of zero osmotic pressure. This means that the shell acts like a simple harmonic spring with a spring constant of $K_1 = 8\sqrt{\kappa Y}/R$. Nevertheless, by taking into account the osmotic pressure, two springs in series are formed, one originates from the shell elasticity and the other from the inside pressure.

Table 3 summarises the K_1 values calculated for the four bubbles shown in Fig. 2, as well as the slope of their curve (K_{MD})
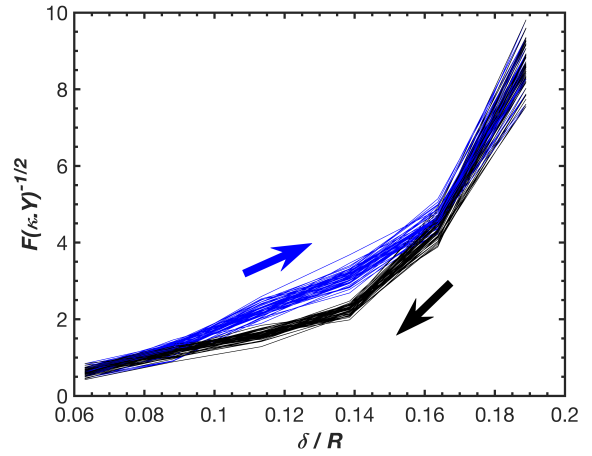

Fig. 3 The force-displacement curve for periodic indentation after 50 cycles for a Ne bubble with number of trapped atoms $N_t = 800$ at room temperature. The bubble is resilient against fatigue. Irreversibility in the curves develops after the partial buckling transitions resulting in hysteresis in the curves.

Table 3 Force-deformation curves slope calculated from MD and continuum theories

N_t	800		1100	
Gas	He	Ne	He	Ne
K_{MD} (N/m)	88.66	98.23	56.49	82.44
$K_{1,TST}$ (N/m)	25.27	21.57	21.58	18.20
$K_2 = \pi PR$ (N/m)	13.48	16.69	14.17	16.77

before the first buckling transition where the curves are linear. Comparing the results, we see that TST relatively underestimates the slope of the curves, however the values are still of the same order of magnitude.

One should note that our nano bubbles are not perfect spheres which violates the initial assumption of Eq. 1. Moreover, the bubbles support hydrostatic pressures of the order of GPa (see the trapped materials: pressure and aggregation state). Therefore, the calculated K_1 values from TST, while neglecting the osmotic pressure, are expected to underestimate the slope of the curves.

Comparing the K_{MD} results, we can see that the values for $N_t = 800$ are higher than for $N_t = 1100$. The low N_t bubbles have smaller radius, thereby having higher shell spring constant as is evident in the K_1 formula. Nevertheless, the K_{MD} values of the Ne atoms are clearly larger than for the He bubbles, even comparing the Ne bubble of $N_t = 800$ and He bubble of $N_t = 1100$ whose shape were rather identical (refer to table 2). We will show in the followings that, for the same N_t, the trapped materials hydrostatic pressure are distinctly larger for the Ne bubbles than for the He bubbles. Hence, the higher K_{MD} values for the Ne bubbles further emphasises the significance of the spring originating from the trapped materials hydrostatic pressure.

Alternatively, using the analytical methods of ref. 34, the force-deformation slopes (F/δ) can be estimated as $K_2 = \pi PR$. Values of K_2 for the same bubbles are also summarised in table 3. The latter relation has been obtained by ignoring the shell out of

plane bending energy and we restricted ourselves to the in-plane stretching energy. The length scale κ/Y representing the ratio of the bending to stretching forces is ~ 0.25 Å for graphene, which is far below our smallest bubbles maximum heights (6.4 Å). Therefore, ignoring the bending energy is a reasonable approximation. Arithmetic summation of the K_1 and K_2 values, as two springs in series, would get us closer to the K_{MD} values. We conclude that the TST relations for perfect spheres provides us with a simple interpretation of the force-deformation slopes for small deformation.

Using TST in interpreting the force-deformation slopes after the buckling transitions where the curves exhibit highly nonlinear behaviour involves solving the highly nonlinear sets of differential equations known as the Föppl–von Kármán equations . These equations cannot be solved analytically and necessitates numerical computations such as finite-element analysis which are beyond the scope of our study. This further points out the significance of molecular simulations in studying the mechanics of graphene nano bubbles.

It is worth noting that TST commonly predicts nonlinearity of the force-deformation curves in deformations beyond the length scale $\sqrt{\kappa/Y}$. For our smallest bubble (He bubble of $N_t = 800$), this yields $\delta/R \approx 0.01$, while our nano bubbles exhibited linear behaviour until $\delta/R \approx 0.05$ (see Fig. 2), which further extends the applicability of the continuum theory.

6 The trapped materials: pressure and aggregation state

Graphene nano bubbles have been known to withstand extreme hydrostatic pressures[35]. Since the pressure of the trapped materials originates from the van der Waals adhesion between the graphene sheet and the substrate, it is customary to refer to it as the van der Waals pressure[2]. Next, we calculate the trapped materials hydrostatic pressure during the indentation of the bubbles.

The pressure values were calculated using the stress formulation[36] that was found to be valid for systems even away from either equilibrium or homogeneity. Fig. 4 illustrates the values of the pressures for Ne bubbles versus the tip displacement, for different values of N_t and temperature. The pressure values for He and Ar bubbles are illustrated in supplementary Figs. S13 and S14. It is worth reviewing how the pressure is calculated here. Under hydrostatic condition, a simple force balance for an infinitesimal volume inside the system yields the hydrostatic pressure[36] to be as $P = \frac{1}{3}(\sigma_{xx} + \sigma_{yy} + \sigma_{zz})$ where σ_{xx}, σ_{yy} and σ_{zz} are the internal normal stress components. The normal stress can then be determined with the summation of two terms including: the interatomic forces and the momentum flux due to the inner-diffusion of the atoms.

In the following we will find that the trapped materials of Ne and Ar bubbles are in the solid state, and exhibit a crystalline structure. For He bubbles they are in the liquid state with restricted inter-diffusion. Therefore, atomic movements away from their crystalline lattices are not anticipated, and the bubbles' pressure stems from the first term of the normal stress, that is, the interatomic interactions. Comparing the results, we notice that
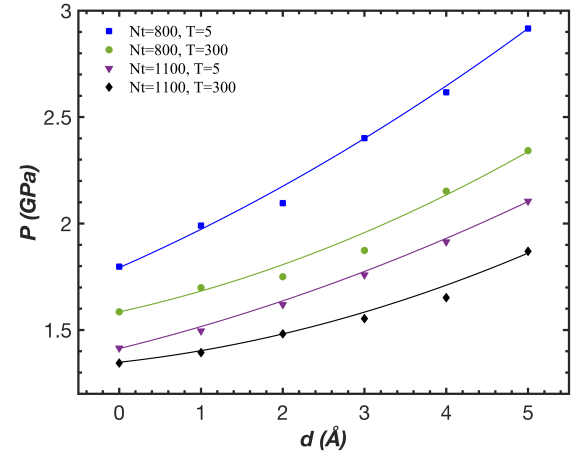

Fig. 4 Trapped materials hydrostatic pressure for Ne bubbles as function of tip displacement for different N_t and temperatures. The curves are guide to the eye.

the pressure of Ne bubbles, for the same N_t, are larger than for He and Ar bubbles. The stronger interatomic interaction of Ne atoms as compared to He atoms results in higher pressure inside the Ne bubbles than He bubbles. Ar bubbles, on the other hand, although have stronger interactions, acquire much larger volumes which suppresses the effect of atomic interactions resulting in a lower pressure of Ar bubbles than Ne bubbles.

Surprisingly, the pressure graphs show that the trapped materials have higher pressure at low temperature than at room temperature. We found in table 2 that the bubble radius is smaller at low temperature. Graphene compresses the trapped materials in the radial direction more at low temperature than at room temperature, and it is as if a substance is subjected to an external compression ensuing normal stresses inside the substance. A possible argument could be that some of the trapped materials are in the solid state, and therefore the force balance of the stress formulation should involve shear stresses as well, as solids, contrary to liquids, withstand shear stresses at equilibrium. Our MD calculations shows shear stresses for all bubbles that are one order of magnitude smaller than the normal stresses, therefore would have minor influence on the force balance.

The pressure values increase with increased indentation. As expected, with increasing external force from the tip, the normal stresses inside the trapped material increases, and consequently the pressure increases. Moreover, we will show in the following that the indentation increases the trapped materials' surface to volume ratio, and the pressure in a solid material is expected to increase with increased surface to volume ratio[37].

To further understand the structure and aggregation state of the trapped materials at room temperature, we calculated the radial distribution function (RDF) and the number density distribution of the trapped materials (in the direction perpendicular to the substrate) for times before the indentation and after the indentation in the last time frames prior to the graphene failure. Fig. 5 (a-c) illustrates the number density distributions before and after the indentation. The graphs exhibit a layered structure. The
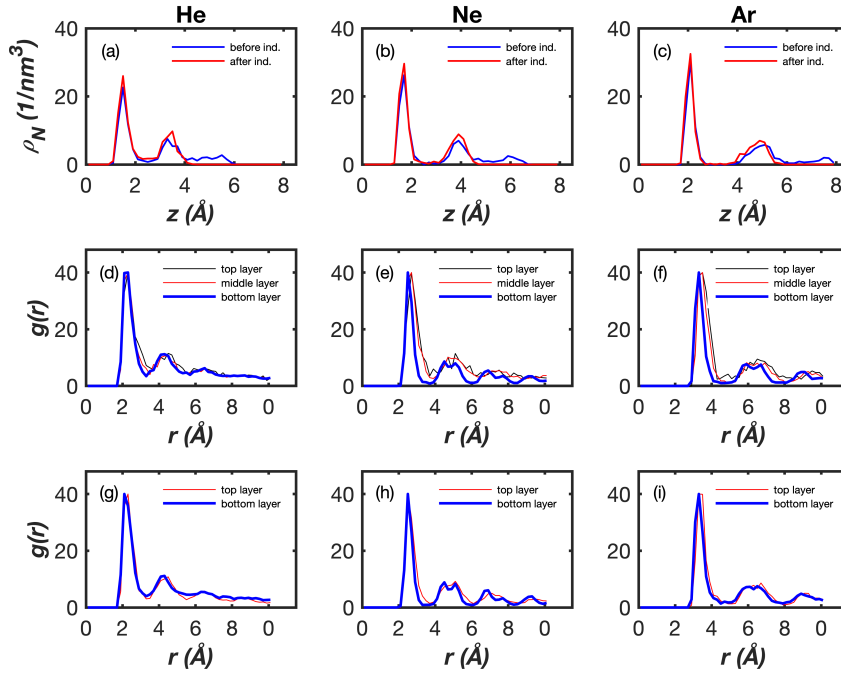
Fig. 5 Number density graphs for bubbles at room temperature before and after the indentation. The trapped materials apparently exhibit a layered structure. Indentation reduces the number of materials layers by one (a-c). Radial distribution function (RDF) for each of the three layers of trapped materials before the indentation (d-f) and the two layers of trapped materials after the indentation (g-i). The He atoms show a liquid state while Ne and Ar atoms exhibit a more crystalline structure.

trapped material has three distinct layers before the indentation which is reduced to two layers upon indentation. This explains the increase of the trapped materials surface to volume ratio.

Fig. 5 (d-f) illustrates the RDF graphs for each of the three layers of the trapped materials (identified in the number density graphs) before the indentation. The curves of the three layers are more or less the same. We depicted the curves for the bottom layers which contain the majority of atoms in each bubble with thicker lines for a better illustration. RDF graphs exhibit only a second peak for He atoms while there are additional peaks for Ne and Ar atoms indicating that He atoms are in the liquid state while Ne and Ar atoms are in the solid states. A look at our MD trajectories confirm that Ne and Ar form a stable crystalline structure, while He show a more disordered atomic arrangement yet with restricted dynamic arrangements (see supplementary movies 2-4). We conclude that Ne and Ar are in the solid state and He is in the liquid state.

Similarly, Fig. 5 (g-i) shows the RDF graphs for the two layers of trapped materials after the indentation. The curves for each material are similar to those before the indentation suggesting that the influence of indentation on the trapped materials' aggregation state is not that significant. The plotted results are for N_t = 800, while the results for N_t = 1100 are very similar.

We compare the trapped materials' pressure with the solidification pressure of their bulk condition. Parameterisations of Simon's law for He[38], Ne[39] and Ar[38] yield solidification pressure at room temperature of P_s = 12.09 GPa for He, P_s = 4.79 GPa for Ne,

and P_s = 1.35 GPa for Ar. Interestingly, the calculated pressure of Ne and Ar bubbles (1.59 GPa and 1.14 GPa, respectively) are below their bulk solidification pressure. We attribute this to the effect of strong confinement which further elucidates the effect of confinement on the materials properties.

Lastly, in order to verify that the solidification results from the effect of confinement and not from the LJ model, we performed a few extra simulations. With the same LJ parameters used here, we simulated Ne and Ar gases in an isothermal-isobaric (NPT) ensemble (at room temperature and the corresponding bubble pressures) within a periodic box. The uncertainty in the prediction of melting lines in LJ models can be attributed to the size effect or the MD interaction cut-off[40]. Therefore, we repeated the simulations with two different numbers of atoms (1100 and 62500), using 1 nm or 2 nm cut-off distances in each case. Supplementary Fig. 15 illustrates RDF graphs for different cases, and supplementary movies 5 and 6 show the Ne and Ar boxes with 1100 atoms and a 1 nm cut-off. The RDF graphs or movies show that the gases are in the liquid state, so we can infer that the solidification of the trapped materials inside the bubbles originates from confinement.

7 Conclusions

We investigated the effect of nano indentation of graphene nano bubbles using molecular dynamics simulation. The bubbles structural failure can be predicted from the elastic properties of graphene and the bubbles radius in terms of the Föppl–von Kármán (FvK) dimensionless number. The continuum elasticity the-

ory of thin shells qualitatively explains the linear response of the bubble against the force applied from the indentation tip. The bubbles do not degrade while being subjected to cycling deformations when below the failure point. Ne and Ar atoms inside the nano-bubble are ordered into a crystalline state for pressures lower than their bulk melting pressure because of the highly confinement. This study sheds light on the important feature of nano-indentation of nano-bubbles.

Acknowledgements

Notes and references

1 A. K. Geim and I. V. Grigorieva, *Nature*, 2013, **499**, 419–425.
2 E. Khestanova, F. Guinea, L. Fumagalli, A. Geim and I. Grigorieva, *Nature Communications*, 2016, **7**, 1–10.
3 S. J. Haigh, A. Gholinia, R. Jalil, S. Romani, L. Britnell, D. C. Elias, K. S. Novoselov, L. A. Ponomarenko, A. K. Geim and R. Gorbachev, *Nature Materials*, 2012, **11**, 764–767.
4 H. Ghorbanfekr-Kalashami, K. Vasu, R. R. Nair, F. M. Peeters and M. Neek-Amal, *Nature Communications*, 2017, **8**, 1–11.
5 R. Nair, H. Wu, P. Jayaram, I. Grigorieva and A. Geim, *Science*, 2012, **335**, 442–444.
6 J. K. Holt, H. G. Park, Y. Wang, M. Stadermann, A. B. Artyukhin, C. P. Grigoropoulos, A. Noy and O. Bakajin, *Science*, 2006, **312**, 1034–1037.
7 J. M. Yuk, J. Park, P. Ercius, K. Kim, D. J. Hellebusch, M. F. Crommie, J. Y. Lee, A. Zettl and A. P. Alivisatos, *Science*, 2012, **336**, 61–64.
8 J. Park, H. Park, P. Ercius, A. F. Pegoraro, C. Xu, J. W. Kim, S. H. Han and D. A. Weitz, *Nano Letters*, 2015, **15**, 4737–4744.
9 K. Xu, P. Cao and J. R. Heath, *Science*, 2010, **329**, 1188–1191.
10 G. Algara-Siller, O. Lehtinen, F. Wang, R. R. Nair, U. Kaiser, H. Wu, A. K. Geim and I. V. Grigorieva, *Nature*, 2015, **519**, 443–445.
11 M. Arnoldi, M. Fritz, E. Bäuerlein, M. Radmacher, E. Sackmann and A. Boulbitch, *Physical Review E*, 2000, **62**, 1034.
12 M. S. Daw and M. I. Baskes, *Physical Review B*, 1984, **29**, 6443.
13 S. J. Stuart, A. B. Tutein and J. A. Harrison, *The Journal of Chemical Physics*, 2000, **112**, 6472–6486.
14 Z. Ni, H. Bu, M. Zou, H. Yi, K. Bi and Y. Chen, *Physica B: Condensed Matter*, 2010, **405**, 1301–1306.
15 O. Shenderova, D. Brenner, A. Omeltchenko, X. Su and L. Yang, *Physical Review B*, 2000, **61**, 3877.
16 K. Dilrukshi, M. Dewapriya and U. Puswewala, *Theoretical and Applied Mechanics Letters*, 2015, **5**, 167–172.
17 M. Dewapriya, A. S. Phani and R. Rajapakse, *Modelling and Simulation in Materials Science and Engineering*, 2013, **21**, 065017.
18 B. Peng, M. Locascio, P. Zapol, S. Li, S. L. Mielke, G. C. Schatz and H. D. Espinosa, *Nature Nanotechnology*, 2008, **3**, 626–631.
19 M. R. Hestenes, E. Stiefel *et al.*, *Methods of conjugate gradients for solving linear systems*, NBS Washington, DC, 1952, vol. 49.
20 T. Zhang, X. Li and H. Gao, *International Journal of Fracture*, 2015, **196**, 1–31.
21 S. Plimpton, *Journal of Computational Physics*, 1995, **117**, 1–19.
22 A. Stukowski, *Modelling and simulation in materials science and engineering*, 2009, **18**, 015012.
23 T. Halicioğlu and G. Pound, *Physica Status Solidi (a)*, 1975, **30**, 619–623.
24 L. A. Girifalco, M. Hodak and R. S. Lee, *Physical Review B*, 2000, **62**, 13104.
25 H. Hippler, J. Troe and H. Wendelken, *The Journal of Chemical Physics*, 1983, **78**, 6709–6717.
26 R. Villarreal, P.-C. Lin, F. Faraji, N. Hassani, H. Bana, Z. Zarkua, M. N. Nair, H.-C. Tsai, M. Auge, F. Junge *et al.*, *Nano Letters*, 2021, **21**, 8103–8110.
27 W. Roos, R. Bruinsma and G. Wuite, *Nature Physics*, 2010, **6**, 733–743.
28 L. D. Landau and E. M. Lifshits, *Theory of Elasticity*, Pergamon Press, 1964.
29 W. S. Klug, R. F. Bruinsma, J.-P. Michel, C. M. Knobler, I. L. Ivanovska, C. F. Schmidt and G. J. Wuite, *Physical Review Letters*, 2006, **97**, 228101.
30 A. Fasolino, J. Los and M. I. Katsnelson, *Nature Materials*, 2007, **6**, 858–861.
31 P. Liu and Y. Zhang, *Applied Physics Letters*, 2009, **94**, 231912.
32 L. Yi, *AIP Advances*, 2018, **8**, 075104.
33 H. Zhao and N. Aluru, *Journal of Applied Physics*, 2010, **108**, 064321.
34 D. Vella, A. Ajdari, A. Vaziri and A. Boudaoud, *Journal of the Royal Society Interface*, 2012, **9**, 448–455.
35 G. Zamborlini, M. Imam, L. L. Patera, T. O. Mentes, N. Stojic, C. Africh, A. Sala, N. Binggeli, G. Comelli and A. Locatelli, *Nano Letters*, 2015, **15**, 6162–6169.
36 D. Tsai, *The Journal of Chemical Physics*, 1979, **70**, 1375–1382.
37 J. Weissmüller and J. W. Cahn, *Acta Materialia*, 1997, **45**, 1899–1906.
38 F. Datchi, P. Loubeyre and R. LeToullec, *Physical Review B*, 2000, **61**, 6535.
39 J. Solca, A. J. Dyson, G. Steinebrunner, B. Kirchner and H. Huber, *The Journal of Chemical Physics*, 1998, **108**, 4107–4111.
40 E. A. Mastny and J. J. de Pablo, *The Journal of Chemical Physics*, 2007, **127**, 104504.